Soft Matter

Liquid Crystalline Networks based on Photo-initiated Thiol-ene Click Chemistry

Journal:	*Soft Matter*
Manuscript ID	SM-ART-09-2019-001818.R1
Article Type:	Paper
Date Submitted by the Author:	26-Nov-2019
Complete List of Authors:	Li, Yuzhan; Oak Ridge National Lab, Materials Science and Technology Division Zhang, Yuehong; Northeast Forestry University Goswami, Monojoy; Oak Ridge National Lab, Computational Chemical Sciences Vincent, Dan; Washington State University Wang, Liwei; washington state university, School of Mechanical and Materials Engineering & Composite Materials and Engineering Center Liu, Tuan; washington state university, School of Mechanical and Materials Engineering & Composite Materials and Engineering Center, ; Beijing University of Chemical Technology, Key Laboratory of Carbon Fiber and Functional Polymers Li, Kai; Oak Ridge National Laboratory, Materials Science and Technology Division Keum, Jong; Oak Ridge National Laboratory, Spallation Neutron Source Gao, Zhenhua; Northeast Forestry University Ozcan, Soydan ; Oak Ridge National Laboratory, Materials Science and Technology Division Gluesenkamp, Kyle; Oak Ridge National Lab, Energy and Transportation Sciences Rios, Orlando; Oak Ridge National Laboratory, Materials Science and Technology Kessler, Michael; North Dakota State University, Mechanical Engineering

SCHOLARONE™
Manuscripts

Liquid Crystalline Networks based on Photo-initiated Thiol-ene Click Chemistry

Yuzhan Li[a,1], Yuehong Zhang[b,1], Monojoy Goswami[c]*, Dan Vincent[d], Liwei Wang[d], Tuan Liu[d], Kai Li[e], Jong K. Keum[f], Zhenhua Gao[b], Soydan Ozcan[g], Kyle R. Gluesenkamp[g], Orlando Rios[a,]*, and Michael R. Kessler[h,]*

[a] Materials Science and Technology Division, Oak Ridge National Laboratory, Oak Ridge, TN 37831, United States
[b] College of Materials Science and Engineering, Northeast Forestry University, Harbin, 150040, China
[c] Computational Sciences and Engineering Division, Oak Ridge National Laboratory, Oak Ridge, TN 37831, United States
[d] School of Mechanical and Materials Engineering, Washington State University, Pullman, WA 99164, United States
[e] Chemical Sciences Division, Oak Ridge National Laboratory, Oak Ridge, TN 37831, United States
[f] Center for Nanophase Materials Sciences, Oak Ridge National Laboratory, Oak Ridge, TN 37831, United States
[g] Energy and Transportation Science Division, Oak Ridge National Laboratory, Oak Ridge, TN 37831, United States
[h] Department of Mechanical Engineering, North Dakota State University, Fargo, ND 58108, United States

*1 Bethel Valley Rd, Oak Ridge, TN 37831, United States
Phone: (865) 574-6843. E-mail: goswamim@ornl.gov
*1 Bethel Valley Rd, Oak Ridge, TN 37831, United States.
Phone: (865) 574-3747. E-mail: rioso@ornl.gov.
*1401 Centennial Blvd, Fargo, ND 58108, United States.
Phone: (701) 231-7494. E-mail: Michael.R.Kessler@ndsu.edu.

Abstract

Photo-initiated thiol-ene click chemistry is used to develop shape memory liquid crystalline networks (LCNs). A biphenyl-based di-vinyl monomer is synthesized and cured with a di-thiol chain extender and a tetra-thiol crosslinker using UV light. The effects of photo-initiator concentration and UV light intensity on the curing behavior and liquid crystalline (LC) properties of the LCNs are investigated. The chemical composition is found to significantly influence the microstructure and the related thermomechanical properties of the LCNs. The structure-property relationship is further explored using molecular dynamics simulations, revealing that the introduction of the chain extender promotes the formation of an ordered smectic LC phase instead of agglomerated structures. The concentration of the chain extender affects liquid crystallinity of the LCNs, resulting in distinct thermomechanical and shape memory properties. This class of LCN exhibits fast curing rates, high conversion levels, and tailorable liquid crystallinity, making it a promising material system for advanced manufacturing, where complex and highly ordered structures can be produced with fast reaction kinetics and low energy consumption.

1. Introduction

Shape memory polymers are a unique class of active materials that exhibit reversible shape changing capabilities under a variety of external stimuli, such as heat, light, solvent exposure, electric fields, and magnetic fields.[1-3] This shape changing capability makes them favorable for a wide range of emerging applications, including actuators, sensors, bio-medical devices, and microrobots.[4-6] Out of the varieties of shape memory polymers, liquid crystalline networks (LCNs) fall in a special category due to the unique coupling between rigid liquid crystalline (LC) domains that helps in self-organization and soft crosslinked network that behaves as polymeric elastomers.[7, 8] In the shape programming process, the macroscopic orientation of the LC domains and the soft polymer network allow for a large dimensional change of LCNs caused by applied external forces. In the shape recovering process, on the other hand, the reversible phase transition of the LC domains and the crosslinked network provide the entropic force for LCNs to return to the original shape.[9, 10] Moreover, LCNs can potentially be used as phase change materials for thermal storage applications due to their temperature dependent reversible phase change properties.[11] The unique combination of soft elasticity and phase behavior also allows for the design of elastocaloric materials for solid state cooling devices.[12, 13] A wide variety of LCNs based on thermally cured systems have been reported, including polysiloxanes and epoxies, and many of these materials showed impressive thermomechanical and shape memory properties.[14-23] However, the curing process of these LCNs typically requires high temperatures and long curing times, consuming significant energy. Alternatively, LCNs based on photo-initiated polymerization of acrylates have been developed, which not only enabled photo-curing but also allowed for the design of LCNs with complex LC orientation.[24-32] While progress has been made to achieve outstanding shape memory properties of LCNs, the highly heterogeneous network structures usually cause broad thermal transitions, limiting shape memory efficiency of these materials.

In recent years, interest in the use of photo-initiated click chemistries, such as the thiol-ene reaction, has grown considerably in designing materials. Thiol-ene chemistry offers advantages including high efficiency (rapid polymerization rate with high conversion), insensitivity to oxygen inhibition, and a versatile curing process (photochemically or thermally).[33, 34] In particular, the high curing rate is especially useful for designing reactive polymer inks for additive manufacturing

as fast reaction kinetics are often required in order for the printed layers to possess sufficient mechanical strength to support subsequent layers.[35-38] Furthermore, the unique combination of step-growth and chain-growth polymerization processes allows the formation of a uniform network structure, resulting in low polymerization shrinkage stress.[39] Several thiol-ene based LCNs, such as thiol-vinyl and thiol-acrylate reactions have been reported recently.[40-44] These LCNs were formulated using a di-functional vinyl or acrylate LC monomer, a di-functional thiol chain extender, and a tetra-functional vinyl or thiol crosslinker. In the case of thiol-vinyl systems, the thiol-ene reaction proceeds through free radical additions, while in thiol-acrylate systems the reaction proceeds through Michael additions.[45] While the thermomechanical and shape memory properties of these LCNs have been extensively studied,[46-50] several fundamental aspects, including the effects of chemical formulation on the LC phase formation and the related thermomechanical properties, are still not fully understood. Based on our previous research on epoxy-based LCNs,[51-53] we explore the possibility of using vinyl-based monomers as an alternative way to prepare LCNs.

In the present work, we report a combined experimental and computational approach to understand the structure-property relationships by investigating main-chain, polydomain LCNs at the nanoscale. A photo-initiated thiol-ene click chemistry was used to prepare LCNs with fast curing speed, high conversion, and uniform network structure. We investigated the LC phase formation during the curing process to understand the effect of reaction conditions, such as initiator concentration, UV light intensity, and chemical composition on the final liquid crystallinity of the LCNs. Employing coarse-grained molecular dynamics (MD) simulations, we further elucidated the effect of the chain extender on the formation and development of the nanoscale LC phase and examined their fundamental properties. Based on the understanding of these structure-property relationships, LCNs with different crosslink density and liquid crystallinity were prepared, resulting in tailored thermomechanical and shape memory properties.

2. Experimental Section

2.1 Materials

Pentaerythritol tetrakis (3-mercaptopropionate) (PETMP, >95%), 2,2-dimethoxy-2-phenylacetophenone (DMPA, 99%), and 4,4’-dihydroxybiphenyl (97%) were purchased from Sigma-Aldrich. 1,4,7,10,13,16-hexaoxacyclooctadecane (18-Crown-6, 99%) and 1,4-bis(mercaptoacetoxy)butane (BMAB, 95%) was obtained from TCI Chemicals. 6-bromo-1-hexene (98%) was obtained from Combi-Blocks. Anhydrous potassium carbonate (K_2CO_3), acetone, and ethanol were purchased from Fisher Scientific. All chemicals were used as received without further purification. The biphenyl-based divinyl monomer (4,4'-Bis(5-hexen-1-yloxy)-1,1'-biphenyl, BPDV) was prepared using the Williamson ether synthesis method (Figure S1 in supplementary information). A mixture of 4,4’-dihydroxybiphenyl (9.516 g, 0.051 mol), 18-Crown-6 (1.351 g, 0.0051 mol), and K_2CO_3 (35.316 g, 0.256 mol) was suspended in 400 ml of acetone in a round bottom flask. Then, 6-bromo-1-hexene (25 g, 0.153 mol) was added into the flask and the reaction mixture was refluxed for 24 h. After the reaction, the hot solution was filtered, and the filtrate was concentrated using a rotary evaporator. The precipitate was washed successively with water and ethanol yielding white flakes. The product was dried at 50 °C under vacuum and was used without further purification (14.865 g, dry yield 83.1%). ^{1}H NMR (DMSO-d_6): δ = 7.51–7.53 (d, 4H), 6.97–6.99 (d, 4H), 5.79–5.89 (m, 2H), 4.96–5.07 (m, 4H), 3.99–4.02 (t, 4H), 2.08–2.13 (m, 4H),

1.70–1.77 (m, 4H), 1.49–1.56 (m, 4H). ^{13}C NMR (DMSO-d_6): δ = 157.94, 138.80, 132.43, 127.40, 115.19, 115.01, 67.47, 33.08, 28.39, 24.98.

2.2 Preparation of LCN films

PETMP, BMAB, and BPDV in different molar ratios were mixed while maintaining an equivalent amount of thiol and vinyl groups. 1 wt% of DMPA was added to the mixture as a photo-initiator (Figure S2a in supplementary information). The powder mixture was transferred into a glass vial and melted at 130 °C in an oil bath. Once melted, the mixture was manually stirred for 5 min. Prior to casting of the films, a square glass open-faced mold was spray-coated with a thin layer of PTFE and equilibrated to 130 °C on a hot plate. The dimension of the glass mold is L*W*H = 50mm*50mm*5mm (Figures S2b and S2c in supplementary information). The dimension of the indent in the center of the glass mold for holding materials is L*W*H = 25mm*25mm*1mm. The mold release lubricant was MR 311 Dry Film Release Agent and was purchased from McMASTER-CARR. The thickness of the applied mold release agent was estimated to be 50 μm. The liquid mixture was then poured into the mold and equilibrated for 90 s. A clean glass slide was then placed over the mold while leaving one small corner of the mold face uncovered. This small gap was left open to allow for some contraction of the material during the curing reaction. Next, a UV light source centered directly above the mold was turned on for 2 min with an intensity of 5 mW/cm^2 at the mold face to activate the photo-initiator and polymerize the samples. After that, the mold was removed from the hot-plate and allowed to cool to room temperature to obtain the polymerized LCN films with a dimension of L*W*H = 50mm*50mm*5mm. The prepared LCN films with different compositions were labeled as LCN-102, LCN-113, LCN-124, LCN-146, and LCN-168, as shown in Table 1.

Table 1 LCNs with different chemical compositions

	PETMP (mol)	BMAB (mol)	BPDV (mol)	Mole fraction of PETMP (%)
LCN-102	1	0	2	33.3
LCN-113	1	1	3	20.0
LCN-124	1	2	4	14.3
LCN-146	1	4	6	9.1
LCN-168	1	6	8	6.7

2.3 Characterization

The chemical structure of the synthesized BPDV was characterized using proton and carbon nuclear magnetic resonance (^{1}H and ^{13}C NMR). Tests were carried out at room temperature using a Bruker DRX 400 NMR instrument with DMSO-d_6 as the solvent. NMR data was analyzed using the Mnova software from Mestrelab Research S.L. The thermal and LC behavior of BPDV was studied using a differential scanning calorimeter (DSC) from TA Instruments. Samples were tested using a Discovery DSC with heat-cool-heat cycle from -50 to 150 °C at a scanning rate of 10 °C/min under a nitrogen purge of 20 mL/min. The first heating scan was used to erase the thermal history, and the second heating scan was used to analyze the thermal behavior. Non-ambient X-ray diffraction (XRD) was performed using PANalytical X'Pert Pro equipped with TTK-450 heating stage to investigate the structure changes of the monomer related to the thermal

transitions. Diffraction patterns were collected at 27 ℃, 85 ℃, 150 ℃ on heating process and 85 ℃, 27 ℃ on cooling process, respectively, at a scan rate was 0.15°/min over a 2θ from 0° to 60°.

The curing behavior of the LCNs was investigated using the DSC equipped with a UV light source (OmniCure S2000). Approximately 10 mg of an uncured sample was loaded into a DSC pan without a lid and equilibrated at 125 °C in the DSC cell until the heat flow reading of the DSC became stable. The UV light was then turned on and the generated heat flow was recorded for 3 min. After the photo-DSC tests, the thermal and LC properties of the cured LCN samples were studied by running a heat-cool-heat dynamic DSC scan. The curing behavior was also characterized using a NICOLET iS50 Fourier Transform Infrared Spectroscopy (FTIR) system in attenuated total reflectance (ATR) mode to monitor the conversion of thiol and vinyl groups. Dimond was used as the ATR crystal. FTIR spectra were collected at 4 cm^{-1} resolution using 64 scans from 4000 to 400 cm^{-1} and corrected against ambient air as background.

For the prepared LCN films with different compositions, the thermal and LC properties were characterized using a heat-cool-heat dynamic DSC scan. DSC measurements of the LCN films were performed using the same procedure used for characterizing the monomer. The glass transition temperature (T_g), LC phase transition temperature (T_{lc}), and enthalpy of the phase transition (ΔH_{lc}) were determined from the second heating scan. The dynamic mechanical properties of the LCNs were characterized using a model Q800 dynamic mechanical analyzer (DMA) from TA Instruments. Rectangular LCN films with 5mm width and 1mm thickness were used for the DMA tests (oscillation, tensile, and shape memory). The length of the tested area of the samples was determined by the distance of the clamps and was 10mm. The LCN films were heated from -50 to 280 °C at 3 °C /min, under an oscillation frequency of 1 Hz, and at an amplitude of 25 μm in a tension mode. Static tensile tests were performed using the DMA. The LCN films were equilibrated at a temperature of 20 °C below their respective clearing point for 5 min, and then uniaxially stretched at a stress ramp rate of 0.2 MPa/min. DSC and DMA data were analyzed using the TRIOS software from TA Instruments. The LC structure of the LCN-146 at strain values of 0 and 200% was examined ex-situ using wide-angle X-ray scattering (WAXS). The X-ray scattering measurements were carried out using an Anton Paar SAXSess mc2. The X-rays were generated at 40 kV/50 mA, and the wavelength of the used X-ray beam was $\lambda = 1.541$ Å (Cu Kα radiation). For wide-angle measurements, a sample-to-detector distance of 44.5 mm was used. The scattering patterns were recorded on a MultiSensitive Phosphor Screen, which were then digitized using a Cyclone Plus Storage Phosphor Scanner (Perkin Elmer). To study shape memory properties of the LCNs, cyclic thermomechanical tensile tests were carried out using the DMA in a controlled force mode. The strain of the LCNs was measured continuously under a constant stress of 0.1 MPa while the temperature was cycled between 70 to 150 °C at 2 °C/min.

2.4 Molecular Dynamics Simulation

Two sets of model coarse-grained polymer chain were constructed to simulate the LCNs prepared with and without the chain extender, as shown Figure S5a. The center benzene ring is represented by 3 coarse-grain beads (red) connected by two stiff bonds with a bond angle of 180º. The first, 'small-chain' system consists of 15 beads, while the second, 'large-chain', system has 35 beads in each chain. In the experiments, the increase in BMAB concentration increased the length of the oligomers by chemically extending the chain, and hence we utilized the short and long chain polymers to computationally model systems technically equivalent to the experiments. For small-chain and large-chain systems, total 8000 and 3429 chains were simulated respectively. To keep

the density constant, smaller number of chains were used in the large-chain system. Monomer sizes, represented by σ, were kept the same, but mass was normalized to CH_2 mass. Figure S5b represents randomly generated initial system. The simulations were performed on the randomly generated initial system as shown in Figure S5b. The central simulation cell size was 53x53x53 in reduced unit. Considering one reduced unit approximately 0.5 nm, the system size can be approximately 27 nm. Periodic Boundary Conditions (PBC) were used on all three dimensions. The simulations are performed using LAMMPS MD package. The details of the MD simulations are given in supporting information (Section S2).

3. Results and Discussion

3.1 Synthesis of monomer and formulation of LCNs

The divinyl monomer (BPDV) was prepared using the Williamson ether synthesis method. The details of the synthetic route and NMR spectra of the synthesized monomer are shown in Figure S1. From the DSC thermogram of the synthesized BPDV (Figure 1b), we observed the monomer exhibiting two endothermic peaks at 50.1 and 119.4 °C, respectively, during the heating process. The first peak was caused by the change of crystal structure of the monomer as it remained solid after the thermal transition. The second peak was attributed to the melting point of BPDV. Upon cooling, two exothermic peaks were observed, corresponding to the two transitions in the heating process. No LC phase was observed on either heating or cooling as confirmed by the lack of birefringence under polarized light, indicating a non-LC nature of the monomer. To correlate the thermal transitions with structure changes of the monomer, high temperature XRD experiments were performed at 27 ℃, 80 ℃, 150 ℃ on heating and 80 ℃ and 27 ℃ on cooling. The XRD spectra are shown in Figure 1c. A change of crystal structure was observed when the monomer was heated to 80 ℃, as indicated by the shift of the XRD peaks and the formation of new peaks. When heated to 150 ℃, the monomer lost all the short-range order, indicating a molten state. After cooled to 80 ℃ and further to 27 ℃, the intermediate and the original XRD spectra were recovered, respectively.

In the preparation of LCNs, the formation of a network structure has significant influence on the stability of an LC phase, especially when LCNs are synthesized using a non-LC monomer where the LC phase formation and crosslinking are considered competing reactions. Hence, we used a chain extender BMAB to promote the formation of an LC phase (Figure 1a). Unlike the commonly used chain extender, (2,2′-(Ethylenedioxy)diethanethiol, EDDET), BMAB possesses a glycolate esters structure, leading to a higher reaction rate due to weakened sulfur-hydrogen bond resulting from the hydrogen bonding between the thiol and ester carbonyl groups.[39] The increased reaction rate allowed for a higher reaction probability between BPDV and BMAB, thereby facilitating the rigid molecules to organize into an ordered LC phase. To further elucidate the structure-property relationship, experimental factors affecting the curing reaction, such as initiator concentration and UV light intensity, were investigated by curing a small amount of sample in a DSC pan. Following the photo-curing experiments, thermal and LC properties of the LCNs were examined by dynamic DSC scans.

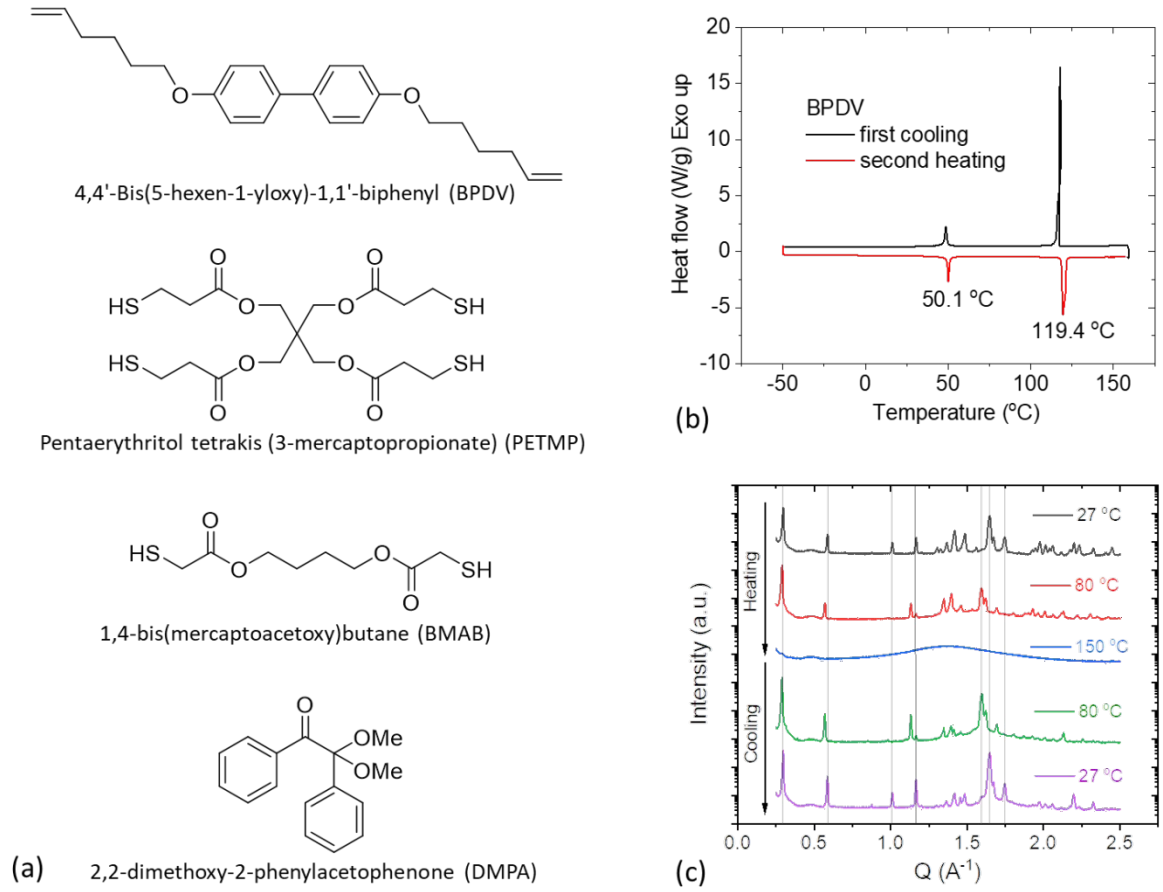

Figure 1. Synthesis of LCNs. (a) Chemical structure of the divinyl monomer BPDV, the tetra-thiol crosslinker PETMP, and the di-thiol chain extender BMAB. (b) DSC thermogram of the synthesized BPDV monomer showing a solid-solid phase transition at 50.1 °C and solid-liquid phase transition at 119.4 °C. Samples were scanned at a heating and cooling rate of 10 °C/min. (c) XRD spectra of BPDV at different temperatures showing two reversible structure changes.

3.1.1 Effect of initiator concentration and UV intensity

The effect of initiator concentration on the curing behavior of the LCNs was studied using a fixed composition (LCN-146) and a fixed UV intensity of 11 mW/cm^2. As can be seen from Figure 2a, the curing reaction started as soon as the UV light was turned on even for the LCN sample without a photoinitiator. This unexpected behavior might be caused by the decay of the thiol groups in BMAB or PETMP that generated thiyl radicals upon the exposure of the UV light.[54] However, for the LCNs cured with a photoinitiator, nearly all of the reaction was completed within 60 s. Interestingly, the heat of reaction decreased with increasing concentration of the photoinitiator, which was attributed to the reduction of liquid crystallinity because of the high crosslinking rate when more photoinitiator was present in the system. In our previous studies on the cure kinetics of liquid crystalline epoxy resins, it was found that the formation of an LC phase resulted in a decrease in activation energy, leading to higher degree of reaction.[55, 56] Figure 2b shows dynamic DSC scans of the LCNs cured with different initiator concentration, where T_{lc} and ΔH_{lc} were determined as the peak temperature of the phase transition and the associated enthalpy,

respectively. Detailed values of T_{lc} and ΔH_{lc} are summarized in Table 2. A reduction of liquid crystallinity was observed with the increasing initiator concentration, which agrees with heat of reaction values determined from the photocuring experiment.

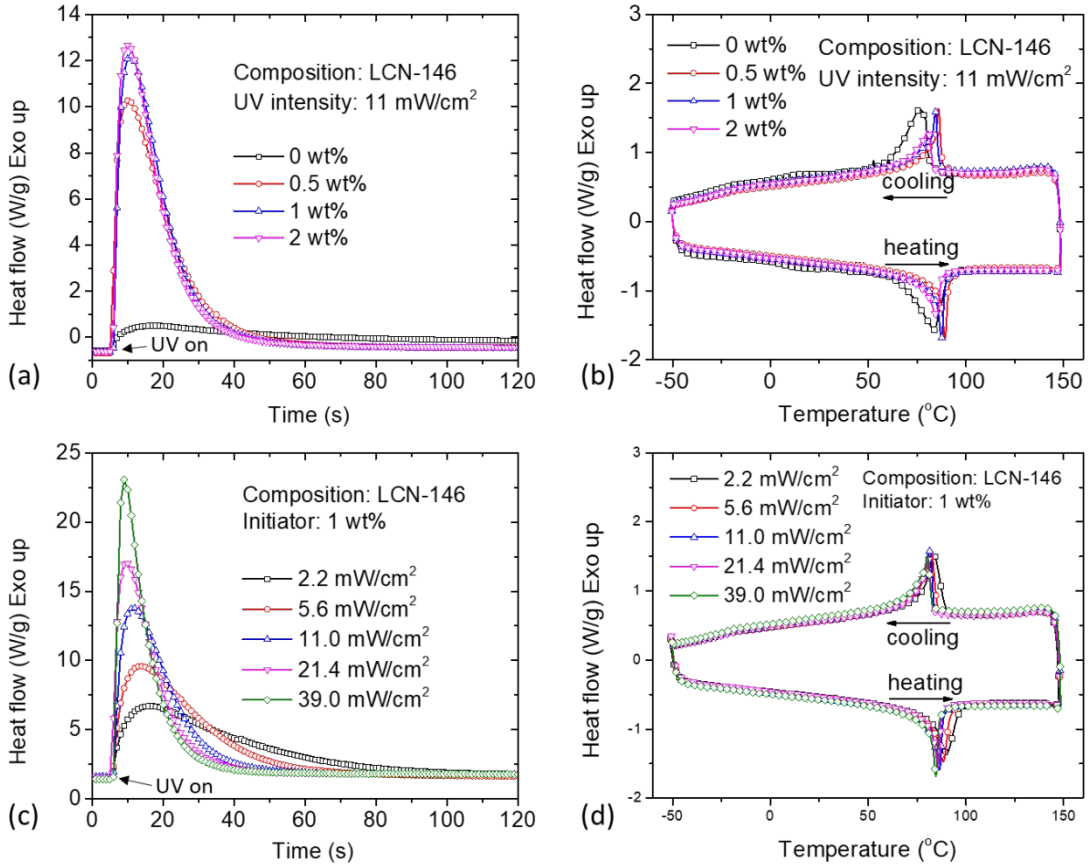

Figure 2. Effect of initiator concentration and UV intensity on thermal and LC properties of the LCNs. (a). DSC curing curves of a model LCN-146 system photo-cured at 11 mw/cm^2 with different initiator concentrations. (b) Dynamic DSC scans of the LCN-146 samples with different initiator concentrations. (c) DSC curing curves of a model LCN-146 system photo-cured at an initiator concentration of 1 wt% at different UV intensities. (d) Dynamic DSC scans of the LCN-146 samples cured at different UV intensities.

Table 2. Effect of initiator concentration and UV intensity on cure behavior and LC properties of a model LCN-146 system.

Effect of Initiator Concentration

Initiator concentration (wt %)	Heat of reaction (J/g)	T_{lc} (°C)	ΔH_{lc} (J/g)
0	22.9	83.9	44.2
0.5	215.3	89.3	26.6
1.0	207.0	87.5	24.6
2.0	196.6	84.8	22.1

Effect of UV Intensity

UV intensity (mW/cm^2)	Heat of reaction (J/g)	T_{lc} (°C)	ΔH_{lc} (J/g)
2.2	174.9	90.0	31.7
5.6	204.5	88.4	28.8
11.0	208.1	86.5	25.6
21.4	210.2	85.8	24.8
39.0	215.1	84.7	24.5

Similar to the study of initiator concentration, the effect of UV intensity on the curing behavior of the LCNs was investigated using a fixed composition (LCN-146) and a fixed initiator concentration of 1 wt%. The DSC curing scans are shown in Figure 2c, the LC properties of the cured LCNs are shown in Figure 2d, and the data determined from the DSC results are summarized in Table 2. A higher level of UV intensity led to a faster reaction rate, accelerating the formation of the crosslinked network. This limited the amount of time that the rigid molecules needed to self-assemble into an LC phase, resulting in a reduction of liquid crystallinity.

3.1.2 Effect of composition

In order to study the effect of chemical composition on the thermal and LC properties of the LCNs, LCN films with different compositions were synthesized by varying the molar ratio of the crosslinker, chain extender, and monomer. The initiator concentration and UV intensity were fixed at 1 wt % and 5.6 mW/cm^2, respectively. First, we studied the thiol-ene reaction using FTIR on a model LCN-146 sample, as shown in Figure 3a and Figure S3 in supplementary information. The absorption peak at 2560, and 1643 cm^{-1} are attributed to the stretching vibration of the S-H bonds and C=C bonds, respectively.[57] Both groups were detected in the uncured LCN-146 system. A shoulder was also observed for the absorption peak at 2560 cm^{-1}, which might be caused by the pre-melting process resulting in a decay of the thiol groups. After UV irradiation, both peaks disappeared in the FTIR spectra, confirming the reaction between the thiol and vinyl groups in the system. Then, we investigated the thermal and LC properties of the LCNs with different compositions. The DSC scans of fully cured samples are shown in Figure 3b. Compared to initiator concentration and UV intensity, the chemical composition showed a greater influence on the thermal and LC properties of the LCNs. For example, LCN-102 exhibited a T_g of 8.9 °C and no LC phase transition was observed. This is attributed to the rapid formation of a highly crosslinked network, inhibiting self-assembly of the rigid molecules. Also, the prepared LCN-102 film was optically transparent (Figure S4 in supplementary information), indicating an amorphous network structure. In the case of LCN-113, the introduction of the chain extender allowed for the formation of a relatively linear oligomer which then self-organized into an LC phase. As a result, a wide, small dip centered at 87.5 °C was observed in the DSC scan, indicating the transition of the LCN from an LC phase to an isotropic phase. However, the LCN-113 film still appeared mostly transparent, suggesting that a limited amount of LC domains were present in the network. As the molar percentage of the chain extender increased, the endothermic peak caused by the LC phase transition became more pronounced because the rigid molecules self-assembled into a highly ordered structure. Both LCN-146 and LCN-168 films were optically opaque because of the light scattering at the boundary between amorphous and liquid crystalline regions. They also exhibited

a large amount of enthalpy related to the LC phase transition, indicating a high degree of liquid crystallinity. In addition, for LCN-146 and LCN-148 samples, the high enthalpy value of the phase transition might be related to crystallization of the alkyl chains as these two samples were more linear than other LCN samples. We observed a 19 ºC drop in T_g from sample LCN-102 to LCN-146. It is worth mentioning that the LC domains greatly restricted the relaxation of polymer chains in the amorphous region, which suppressed the step change in the heat flow signal for LCN-146 and LCN-168 samples, making it difficult to detect T_g of the LCNs from DSC experiments. The DSC results on thermal and LC properties of the LCNs with different compositions are summarized in Table 3. This drastic influence of chemical composition on the LC phase formation stimulated our interest in using molecular dynamics simulations to further understand the structure-property relationships of the LCNs.

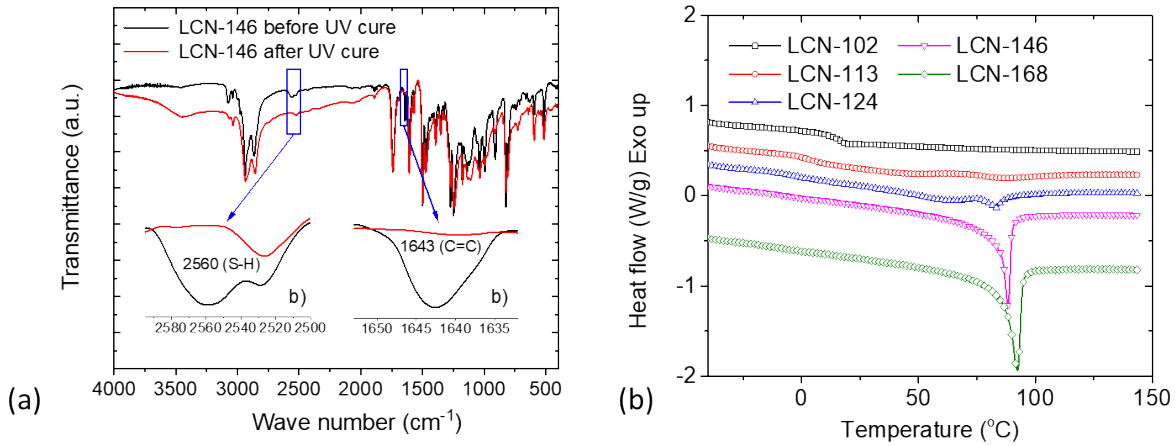

Figure 3. Effect of composition on thermal and LC properties of the LCNs. (a) FTIR spectra of a model LCN-146 system before and after UV curing reaction showing the change of S=H and C=C bonds. (b) Dynamic DSC scans of the LCNs with different compositions.

Table 3. DSC results of the LCNs with different compositions

	Mole fraction of BMAB (%)	T_g (°C)	T_{lc} (°C)	ΔH_{lc} (J/g)
LCN-102	0	14.1	N/A	N/A
LCN-113	20.0	4.1	87.7	2.7
LCN-124	28.6	-2.4	83.3	10.4
LCN-146	36.4	-5.4	88.4	24.0
LCN-168	40.0	N/A	92.3	31.0

3.2 Characterizations of LCNs

3.2.1 Dynamic mechanical properties

The prepared LCN films were investigated using dynamic mechanical analysis to understand the effect of chemical composition on thermal relaxations of the LCNs. Figures 4a and 4b show the change of storage modulus and dissipation factor of the LCNs as a function of temperature.

Transition temperatures, T_g and T_{lc}, were determined from the tan delta curves and are tabulated in Table 4. For all the compositions tested, two consecutive thermal relaxations were observed and were attributed to the glass transition of the amorphous region and the phase transition of the LC region, respectively. The presence of the LC domains significantly influenced dynamic mechanical properties of the LCNs. Below the glass transition temperature, LCNs with higher liquid crystallinity showed an increased elastic behavior with higher values of storage modulus in the glassy region even though the mole fraction of the rigid BPDV molecules in the system was decreased. As the LCNs passed through the glass transition, the LC domains remained stable, restricting the motion of the polymer chains in the amorphous region. It can be seen in Figure 4a that LCNs with higher liquid crystallinity exhibited a smaller drop of storage modulus as the materials went through the glass transition. However, after the LC phase transition, the LC domains no longer existed, and the materials changed into an isotropic phase and behave like traditional rubbers. At this point, the storage modulus of the LCNs were solely influenced by the crosslink density of the materials. In the process of the LC phase transition, an abrupt drop and recovery of the storage modulus was observed for the LCNs. This was caused by the alignment of the LC domains in response to the applied oscillating stress. The behavior was more noticeable for LCN-113 and LCN-124, which was related to the relatively low rigidity and liquid crystallinity of these two compositions.

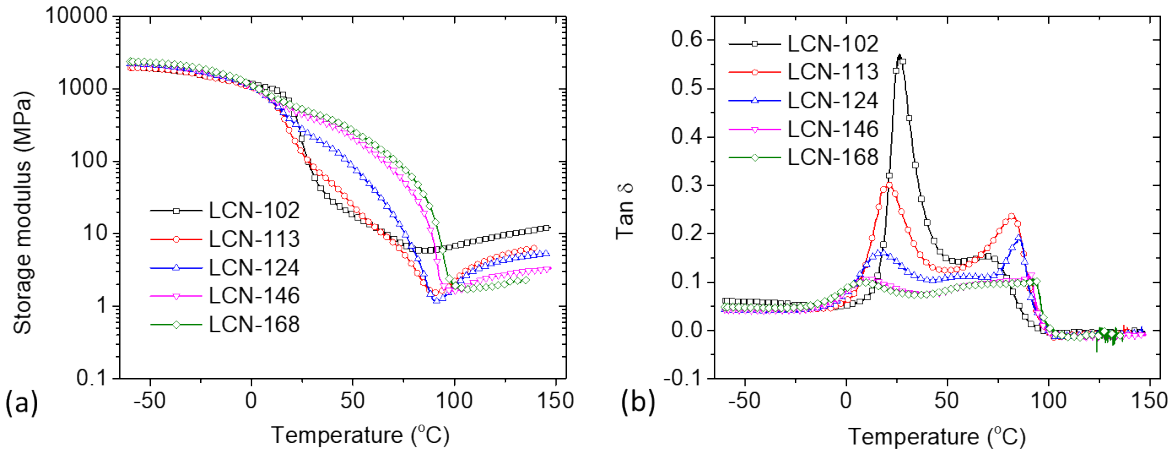

Figure 4. Effect of composition on dynamic mechanical properties of the LCNs. (a) Storage moduli of the LCNs with different compositions determined from oscillating dynamic mechanical tests. (b) Dissipation factor of the LCNs with different compositions determined from oscillating dynamic mechanical tests.

Table 4. DMA results of the LCNs with different compositions

	Mole fraction of BPDV (%)	T_g (°C)	T_{lc} (°C)	Storage modulus at -50 °C (MPa)	Storage modulus at 130 °C (MPa)
LCN-102	66.7	26.3	69.8	1917	9.6
LCN-113	60.0	20.9	82.2	1903	5.2
LCN-124	57.1	17.1	85.5	2155	4.3
LCN-146	54.5	11.4	91.3	2248	2.8
LCN-168	53.3	8.3	92.4	2312	2.0

3.2.2 LC structure and thermomechanical properties

To fully understand the microstructure of the LCNs, including their LC ordering and orientation, 2D WAXS experiments were performed. LCN-146 was used as a model system and the scattering pattern of the as-prepared film is shown in Figure 5a, indicating the presence of a layered smectic ordering. The LCN film was then uniaxially stretched to a strain of 200 % at 71 °C (between T_g and T_{lc}) to induce a LC orientation. The strain was preserved by cooling the material to room temperature, and the resulting orientation was examined ex-situ (Figure 5b). After orientation, the inner scattering rings (q = 1.95, 3.98, and 7.99 nm^{-1}) split into two sets of scattering arcs, implying the formation of a chevron smectic C LC phase (schematically shown in Figure 5c). The two observed orientation axes corresponded to the tilted smectic layers.[58, 59] The outer rings (q = 14.26, 16.27, and 19.48 nm^{-1}), on the other hand, split into two scattering arcs in the equatorial direction, indicating that the long axis of the mesogens as well as the hydrocarbon chains were oriented in the strain direction. The multiple outer rings also indicated the presence of semi-crystalline regions formed by the hydrocarbon chains. The 2D scattering patterns were quantified by integrating along the q direction (Figure 5d). The azimuthal scan at q = 3.98 nm^{-1} was shown in Figure 5e to demonstrate the orientation of the LCNs. Order parameter of the aligned LCN was calculated according to Herman's method,[60] which was determined to be 0.25 at 200 % strain.

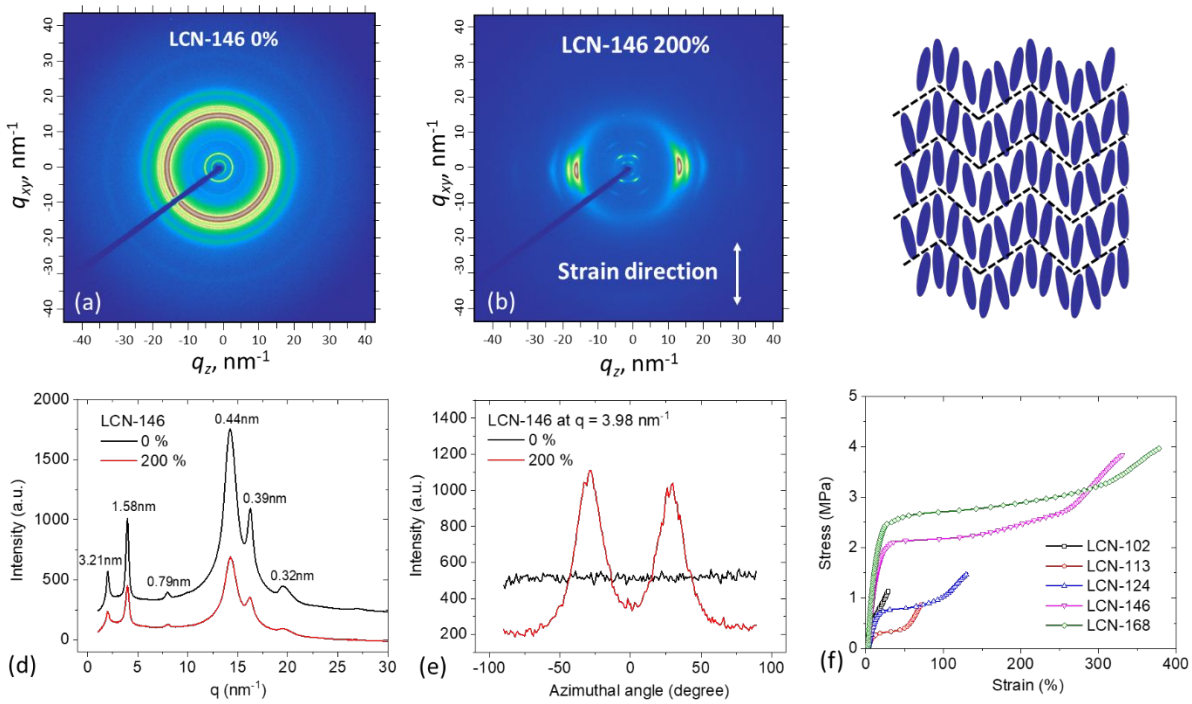

Figure 5. Structural characterization of a model LCN-146 system. (a) WAXS of the LCN-146 film without strain. (a) WAXS of the LCN-146 film with a strain of 200 %. (c) Schematic illustration of the chevron smectic C LC structure. (d) Quantified WAXS data of the LCN-146 films with and without strain. (e) Azimuthal intensity distribution of the scattering peak at q = 3.98 nm^{-1} showing uniaxial orientation of the LCN. (f) Stress-strain behavior of LCNs with different compositions.

One of the interesting properties of LCNs is their soft elasticity which is enabled by the reorientation of the LC domains under small applied forces. As discussed in the previous sections, the composition of the LCNs significantly influenced their LC structure. This difference in liquid crystallinity is apparent in their mechanical behavior during static tensile tests, as shown in Figure 5f. LCNs with higher liquid crystallinities generally exhibited higher strain values at break and longer plateau regions in the stress-strain curves, owing to the large number of LC domains capable of changing orientation in response to the applied uniaxial force. Figures 6a and 6b illustrate the reversible shape change of the LCNs by combining their macroscopic orientation and reversible phase transition characteristics which are responsible for elongation and contraction in a thermomechanical tensile test, respectively. Generally, the LCNs showed reliable shape memory behavior but a slight difference in the strain values was observed due to the difference in liquid crystallinity.

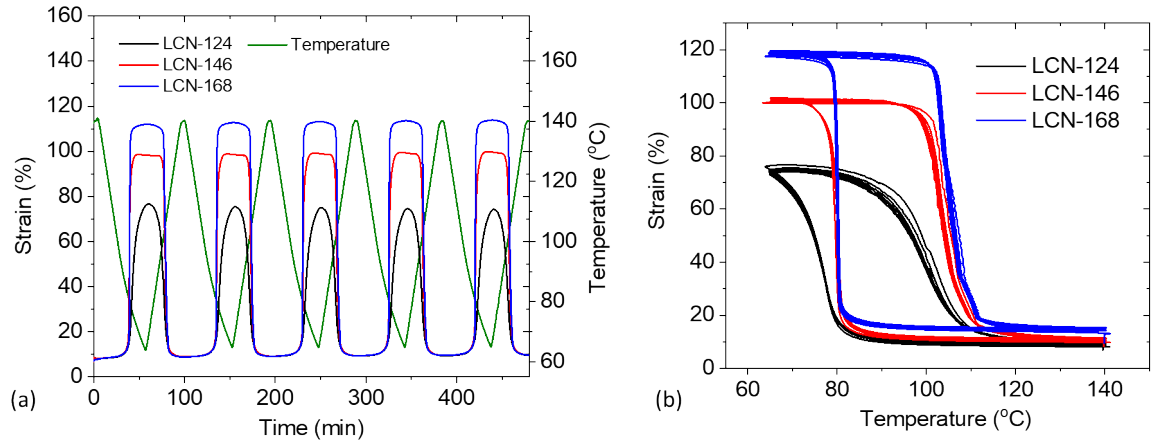

Figure 6. Thermomechanical properties of the LCNs. (a) Cyclic thermomechanical tensile test of LCN-124, LCN146, and LCN-168 showing reversible shape change of the materials. (b) Cyclic thermomechanical tensile test of LCN-124, LCN146, and LCN-168 showing the effect of composition on actuating strain of the materials.

3.3 Molecular Dynamics Simulations

To augment our understanding of the structure-property relationships, we explored the structural details of the LCNs using MD simulation. We argued in Section 3.1 that an increase in BMAB concentration facilitated the assembly of the rigid molecules into a highly ordered LC phase. Structurally we observed the layered LC structures (2D WAXS pattern in Figure 5) for the LCN-146 sample, however, it is not clear whether LCNs with lower BMAM concentration would show more agglomeration or LC ordering. To understand the effect of BMAB concentration, MD simulations (Figure 7) were performed for two different scenarios, a large-chain and a small-chain LCN representing higher and lower concentration of BMAB, respectively.

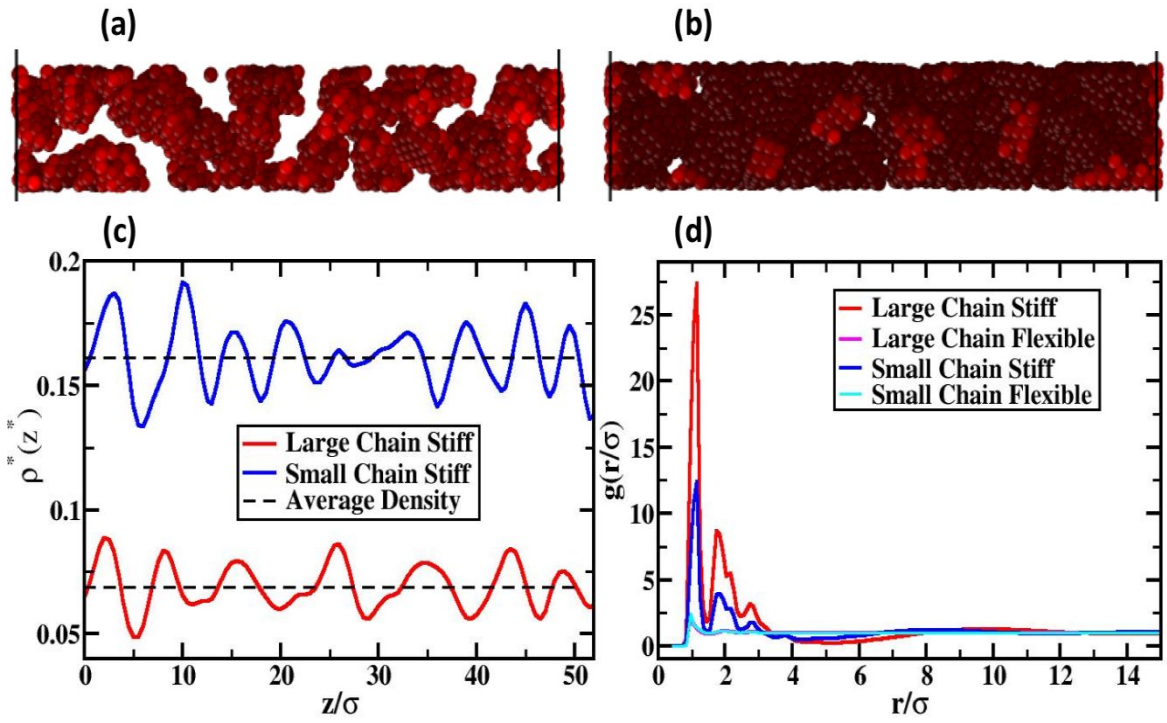

Figure 7. Molecular dynamics simulation showing the effect of BMAB on LC formation. (a) Snapshot of the large-chain length LCN. (b) Snapshot of the small-chain length LCN. (c) Density distribution along z-axis of the stiff mesogens of the LCNs. Density distribution of large-chain LCN (red) showed ordered LC layers of density profile, but the small-chain LCN (blue) showed some breakdown of the LC ordering. (d) Radial distribution function for stiff mesogens and flexible chains for both large-chain and small-chain systems.

The coarse-grain MD simulations of LCNs with different chain lengths showed structurally different morphologies (Figures S5-9 in supporting information). The mesogens interacted with each other via attractive LJ potential, thereby introducing anisotropy at the monomer level that can result into LC ordering (Force-field details can be found in supporting information). A slice of the cross-section of the mesogens along the LC director are shown in Figures 7a and 7b for large-chain and small-chain LCN systems, respectively. While distinct LC ordering was observed in large-chain system (Figure 7a), the same was absent in small-chain system (Figure 7b) where agglomerated structures were observed. The LC ordering was further established from the density wave of the mesogens (Figure 7c) along the director axis, a typical representation of smectic LC ordering.[61] The rigid mesogens showed well-spaced smectic phase ordering for large-chain LCN with a higher BMAB concentration (red lines), however, the same ordering was broken in small-chain LCN with a lower BMAB concentration (blue lines). These findings are commensurate with the experimental WAXS and DSC observations. The radial distribution function (RDF) further elucidates the orientation and long-range order (Figure 7d) of the rigid mesogens. RDF of the flexible chains (cyan and brown lines) showed first and second peaks at 0.97σ and 1.95σ, representing side-by-side monomeric distance and next nearest neighbor peaks, however, no long-range structure was observed. In contrast, RDF of the rigid mesogens for both large (red line) and small (blue line) chain LCNs showed long range structures, as evident by peaks at a longer length-scales. However, for the small-chain LCN stronger agglomeration of the rigid mesognes was

observed. This indicated that the higher order orientational ordering was facilitated by large-chain LCN, consistent with the experiments where LCNs with higher concentration of BMAB showed better LC properties. The large and small chain LCNs both showed peaks near 1.12σ, representing excluded volume peak (LJ repulsion distance) that corresponded to side-by-side packing of the mesogens. The peaks at the longer length scales showed an interval of equally-spaced monomeric distance of 0.97σ, representing a three-dimensional packing of rigid mesogens coming from multiple chains, consistent with the WAXS pattern in Figure 5. The simulation analysis along with the WAXS confirmed the orientational ordering of the LCNs, in which the LC directors were formed by rigid mesogens from multiple chains that in turn assembled into a layered smectic LC structure.

4. Conclusion

We presented an alternative and simple synthesis pathway for the preparation of LCNs using photo-initiated thiol-ene click chemistry. By using the Williamson ether synthesis method, a biphenyl-based di-vinyl monomer was readily prepared in high yield and purity. A tetra-thiol crosslinker and a glycolate ester-based di-thiol chain extender were incorporated to formulate the LCNs. The effects of initiator concentration, UV intensity, and chemical composition on thermal, liquid crystalline, and structural properties of the LCNs were investigated in detail to establish structure-property relationships. Molecular dynamics simulations were performed to provide physical understanding of the effect of the chain extender on LC phase and network formation of the LCNs at the molecular level. It was observed that the chemical composition had dramatic influence on the LC phase formation and the resulting thermomechanical properties. An increase in chain extender boosted the ordering of the LC phase in the LCN as observed from the WAXS data. The ability to control the microstructure of the LCNs allowed us to tailor shape memory behavior of the materials. The fast curing rate and uniform network structure of the LCNs enabled by the thiol-ene click chemistry showed potential applications in advanced manufacturing where fast production with low energy consumption can be realized, such as tape coating and light-based additive manufacturing.

Supporting Information

Synthesis and NMR spectra of BPDV (Figure S1), schematic illustration for the preparation of LCN films (Figure S2), label FTIR spectra of uncured and cured LCN-146 (Figure S3), optical appearance of fully cured LCNs (Figure S4), and detailed MD simulation method (Figures S5-S9).

Conflict of Interest: There are no conflicts of interest to declare.

Acknowledgements

This work was supported by the Air Force Office of Scientific Research (Award FA-9550-12-1-0108). The MD simulations were performed at the National Center for Computational Sciences (NCCS) and used resources of the Oak Ridge Leadership Computing Facility (OLCF) at the ORNL, which is supported by the Office of Science of the U.S. DOE under contract number DE-AC05-00OR22725. WAXS and computer simulation studies were conducted at the Center for Nanophase Materials Sciences (CNMS), which is sponsored by the ORNL Scientific User Facilities Division, DOE Office of Basic Research Sciences. In addition, some of the research was sponsored by the

Critical Materials Institute, Building Technologies Office, Office of Energy Efficiency and Renewable Energy, and Advanced Manufacturing Office, under contract DE-AC05-00OR22725 with UT-Battelle, LLC. We also thank the China Scholarship Council (No. 201506600009) for their financial support.

References

1. M. Behl, M. Y. Razzaq and A. Lendlein, *Adv. Mater.*, 2010, **22**, 3388-3410.
2. G. J. Berg, M. K. McBride, C. Wang and C. N. Bowman, *Polymer*, 2014, **55**, 5849-5872.
3. Q. Zhao, H. J. Qi and T. Xie, *Prog. Polym. Sci.*, 2015, **49–50**, 79-120.
4. J. Leng, X. Lan, Y. Liu and S. Du, *Prog. Mater Sci.*, 2011, **56**, 1077-1135.
5. J. Hu, Y. Zhu, H. Huang and J. Lu, *Prog. Polym. Sci.*, 2012, **37**, 1720-1763.
6. M. D. Hager, S. Bode, C. Weber and U. S. Schubert, *Prog. Polym. Sci.*, 2015, **49–50**, 3-33.
7. C. Ohm, M. Brehmer and R. Zentel, *Adv. Mater.*, 2010, **22**, 3366-3387.
8. T. J. White and D. J. Broer, *Nat Mater*, 2015, **14**, 1087-1098.
9. S. Krause, F. Zander, G. Bergmann, H. Brandt, H. Wertmer and H. Finkelmann, *Comptes Rendus Chimie*, 2009, **12**, 85-104.
10. R. S. Kularatne, H. Kim, J. M. Boothby and T. H. Ware, *Journal of Polymer Science Part B-Polymer Physics*, 2017, **55**, 395-411.
11. D. Wu, B. Ni, Y. Liu, S. Chen and H. Zhang, *Journal of Materials Chemistry A*, 2015, **3**, 9645-9657.
12. M. Trček, M. Lavrič, G. Cordoyiannis, B. Zalar, B. Rožič, S. Kralj, V. Tzitzios, G. Nounesis and Z. Kutnjak, *Philosophical Transactions of the Royal Society A: Mathematical, Physical and Engineering Sciences*, 2016, **374**.
13. G. Skačej, *Liq. Cryst.*, 2018, DOI: 10.1080/02678292.2018.1492035, 1-6.
14. M. Camacho-Lopez, H. Finkelmann, P. Palffy-Muhoray and M. Shelley, *Nat Mater*, 2004, **3**, 307-310.
15. A. Sanchez-Ferrer, T. Fischl, M. Stubenrauch, A. Albrecht, H. Wurmus, M. Hoffmann and H. Finkelmann, *Adv. Mater.*, 2011, **23**, 4526-+.
16. B. Donnio, H. Wermter and H. Finkelmann, *Macromolecules*, 2000, **33**, 7724-7729.
17. K. A. Burke and P. T. Mather, *J. Mater. Chem.*, 2010, **20**, 3449-3457.
18. H. Qin and P. T. Mather, *Macromolecules*, 2009, **42**, 273-280.
19. A. Agrawal, A. C. Chipara, Y. Shamoo, P. K. Patra, B. J. Carey, P. M. Ajayan, W. G. Chapman and R. Verduzco, *Nat Commun*, 2013, **4**, 1739.
20. B. Zhu, M. G. Barnes, H. Kim, M. Yuan, H. Ardebili and R. Verduzco, *Sensors and Actuators B-Chemical*, 2017, **244**, 433-440.
21. Z. Pei, Y. Yang, Q. Chen, E. M. Terentjev, Y. Wei and Y. Ji, *Nat. Mater.*, 2014, **13**, 36-41.
22. Y. Li, C. Pruitt, O. Rios, L. Wei, M. Rock, J. K. Keum, A. G. McDonald and M. R. Kessler, *Macromolecules*, 2015, **48**, 2864-2874.
23. Y. Li, O. Rios, J. K. Keum, J. Chen and M. R. Kessler, *ACS Applied Materials & Interfaces*, 2016, DOI: 10.1021/acsami.6b04374.
24. L. T. de Haan, V. Gimenez-Pinto, A. Konya, N. Thanh-Son, J. M. N. Verjans, C. Sanchez-Somolinos, J. V. Selinger, R. L. B. Selinger, D. J. Broer and A. P. H. J. Schenning, *Adv. Funct. Mater.*, 2014, **24**, 1251-1258.

25. S. Iamsaard, S. J. Asshoff, B. Matt, T. Kudernac, J. Cornelissen, S. P. Fletcher and N. Katsonis, *Nature Chemistry*, 2014, **6**, 229-235.
26. L. T. de Haan, C. Sanchez-Somolinos, C. M. W. Bastiaansen, A. P. H. J. Schenning and D. J. Broer, *Angewandte Chemie-International Edition*, 2012, **51**, 12469-12472.
27. S. K. Ahn, T. H. Ware, K. M. Lee, V. P. Tondiglia and T. J. White, *Adv. Funct. Mater.*, 2016, **26**, 5819-5826.
28. T. H. Ware, M. E. McConney, J. J. Wie, V. P. Tondiglia and T. J. White, *Science*, 2015, **347**, 982-984.
29. M. E. McConney, A. Martinez, V. P. Tondiglia, K. M. Lee, D. Langley, I. I. Smalyukh and T. J. White, *Adv. Mater.*, 2013, **25**, 5880-5885.
30. L. T. de Haan, A. P. H. J. Schenning and D. J. Broer, *Polymer*, 2014, **55**, 5885-5896.
31. C. L. van Oosten, C. W. M. Bastiaansen and D. J. Broer, *Nat Mater*, 2009, **8**, 677-682.
32. A. H. Gelebart, D. J. Mulder, M. Varga, A. Konya, G. Vantomme, E. W. Meijer, R. L. B. Selinger and D. J. Broer, *Nature*, 2017, **546**, 632-+.
33. A. B. Lowe, *Polymer Chemistry*, 2010, **1**, 17-36.
34. A. B. Lowe, *Polymer Chemistry*, 2014, **5**, 4820-4870.
35. S. C. Ligon, R. Liska, J. Stampfl, M. Gurr and R. Mulhaupt, *Chem. Rev.*, 2017, **117**, 10212-10290.
36. A. Kotikian, R. L. Truby, J. W. Boley, T. J. White and J. A. Lewis, *Adv. Mater.*, 2018, **30**.
37. M. Lopez-Valdeolivas, D. Q. Liu, D. J. Broer and C. Sanchez-Somolinos, *Macromol. Rapid Commun.*, 2018, **39**.
38. C. P. Ambulo, J. J. Burroughs, J. M. Boothby, H. Kim, M. R. Shankar and T. H. Ware, *Acs Applied Materials & Interfaces*, 2017, **9**, 37332-37339.
39. C. E. Hoyle, T. Y. Lee and T. Roper, *Journal of Polymer Science Part a-Polymer Chemistry*, 2004, **42**, 5301-5338.
40. A. H. Torbati and P. T. Mather, *Journal of Polymer Science Part B-Polymer Physics*, 2016, **54**, 38-52.
41. D. W. Hanzon, N. A. Traugutt, M. K. McBride, C. N. Bowman, C. M. Yakacki and K. Yu, *Soft Matter*, 2018, **14**, 951-960.
42. T. H. Ware, Z. P. Perry, C. M. Middleton, S. T. Iacono and T. J. White, *Acs Macro Letters*, 2015, **4**, 942-946.
43. M. O. Saed, A. H. Torbati, C. A. Starr, R. Visvanathan, N. A. Clark and C. M. Yakacki, *Journal of Polymer Science Part B-Polymer Physics*, 2017, **55**, 157-168.
44. H. Kim, J. M. Boothby, S. Ramachandran, C. D. Lee and T. H. Ware, *Macromolecules*, 2017, **50**, 4267-4275.
45. C. E. Hoyle and C. N. Bowman, *Angewandte Chemie-International Edition*, 2010, **49**, 1540-1573.
46. M. O. Saed, R. H. Volpe, N. A. Traugutt, R. Visvanathan, N. A. Clark and C. M. Yakacki, *Soft Matter*, 2017, **13**, 7537-7547.
47. N. A. Traugutt, R. H. Volpe, M. S. Bollinger, M. O. Saed, A. H. Torbati, K. Yu, N. Dadivanyan and C. M. Yakacki, *Soft Matter*, 2017, **13**, 7013-7025.
48. C. M. Yakacki, M. Saed, D. P. Nair, T. Gong, S. M. Reed and C. N. Bowman, *Rsc Advances*, 2015, **5**, 18997-19001.
49. D. R. Merkel, N. A. Traugutt, R. Visvanathan, C. M. Yakacki and C. P. Frick, *Soft Matter*, 2018, **14**, 6024-6036.

50. A. Azoug, V. Vasconcellos, J. Dooling, M. Saed, C. M. Yakacki and T. D. Nguyen, *Polymer*, 2016, **98**, 165-171.
51. Y. Li, Y. Zhang, O. Rios, J. K. Keum and M. R. Kessler, *Soft matter*, 2017, **13**, 5021-5027.
52. Y. Li, P. Badrinarayanan and M. R. Kessler, *Polymer*, 2013, **54**, 3017-3025.
53. Y. Li, Y. Zhang, O. Rios, J. K. Keum and M. R. Kessler, *RSC Advances*, 2017, **7**, 37248-37254.
54. N. B. Cramer, J. P. Scott and C. N. Bowman, *Macromolecules*, 2002, **35**, 5361-5365.
55. Y. Li and M. R. Kessler, *J. Therm. Anal. Calorim.*, 2014, **117**, 481-488.
56. C. A. Guymon, E. N. Hoggan, N. A. Clark, T. P. Rieker, D. M. Walba and C. N. Bowman, *Science*, 1997, **275**, 57-59.
57. G. Yang, S. L. Kristufek, L. A. Link, K. L. Wooley and M. L. Robertson, *Macromolecules*, 2016, **49**, 7737-7748.
58. S. Dey, D. M. Agra-Kooijman, W. Ren, P. J. McMullan, A. C. Griffin and S. Kumar, *Crystals*, 2013, **3**, 363-390.
59. A. Sanchez-Ferrer and H. Finkelmann, *Macromolecules*, 2008, **41**, 970-980.
60. G. G. Barclay, S. G. McNamee, C. K. Ober, K. I. Papathomas and D. W. Wang, *Journal of Polymer Science Part a-Polymer Chemistry*, 1992, **30**, 1845-1853.
61. G. R. Luckhurst, *Liquid Crystals Today*, 1993, **3**, 3-5.

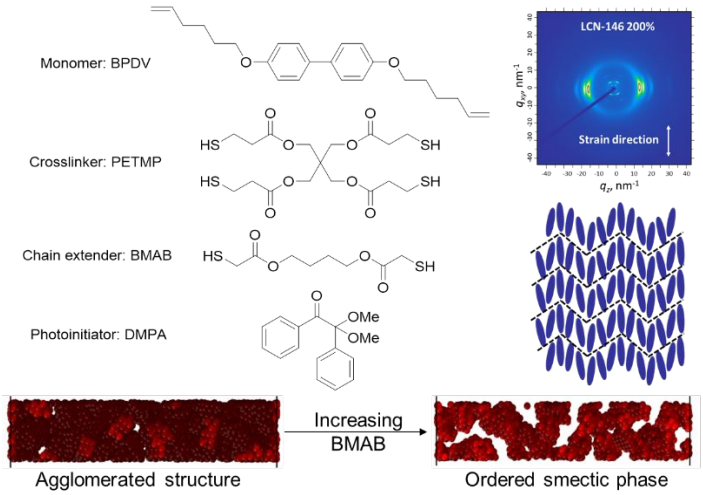

for Table of Contents use only